JOURNAL OF SOLID STATE CHEMISTRY **139,** 152–160 (1998)
ARTICLE NO. SC987823

Hydrothermal Synthesis, Structure, and Characterization of a Mixed-Valent Iron(II/III) Phosphate, $NaFe_{3.67}(PO_4)_3$: A New Variation of the Alluaudite Structure Type

Michael B. Korzenski, George L. Schimek, and Joseph W. Kolis[1]

Department of Chemistry, Clemson University, Clemson, South Carolina 29634-1905

and

Gary J. Long

Department of Chemistry, University of Missouri—Rolla, Rolla, Missouri 65409-0010

Received December 18, 1997; in revised form March 9, 1998; accepted March 17, 1998

A mixed-valent Fe(II/III) phosphate, $NaFe_{3.67}(PO_4)_3$, has been synthesized by high-temperature/high-pressure hydrothermal methods and characterized by single-crystal X-ray diffraction, EDAX, magnetic susceptibility, Mössbauer, infrared, and diffuse reflectance spectroscopies, DTA, and bond valence sum calculations. The compound crystallizes in the monoclinic space group $C2/c$ (No. 15) with $a = 11.881(4)$ Å, $b = 12.564(3)$ Å, $c = 6.522(2)$ Å, $\beta = 115.09(2)^\circ$, $V = 881.7(5)$ Å^3, and $Z = 4$ with $R/R_w = 0.029/0.033$. It exhibits a three-dimensional channel-like structure with an open framework that is similar to the naturally occurring iron-containing mineral alluaudite, $NaFe_3(PO_4)_3$. In alluaudite there are two distinct channels, one which contains the sodium cations and the second which remains empty. In the title phase, this second channel is partially occupied by a square-planar iron atom. The Mössbauer spectral parameters are consistent with the structure and indicate that the fully occupied iron sites are octahedral Fe(II) and the square-planar iron is Fe(III). Structural comparisons to a number of phosphates and arsenates that also possess the alluaudite-type structure, including $NaCu_4(AsO_4)_3$ and $NaMn_4(AsO_4)_3$ are discussed.

INTRODUCTION

Iron phosphates have been studied extensively because of the complex and versatile network structures they can form (1, 2). Iron is of particular interest because it can exist in both the +2 and +3 oxidation states. Iron phosphates have numerous practical applications, including corrosion inhibition (3), passivation of metal surfaces (4), and heterogeneous catalysis (5). Also iron and copper phosphates have shown potential as materials for fossil energy conversion and as sensor materials (6). The recent elegant work by Stucky (7) concerning three-dimensional microporous alkali metal cobalt phosphates prompts us to report recent results concerning a series of new alkali metal and alkaline earth metal iron phosphates prepared in our laboratories. Hydrothermal techniques have proven to be particularly suitable for the synthesis of low-temperature phases and useful for the growth of high-quality crystals (8). Accordingly, we have directed our research toward preparing new ternary iron phosphates from phosphoric acid solutions under hydrothermal conditions. By working in a somewhat higher temperature regime than normally reported, we have synthesized single crystals of the title compound, $NaFe_{3.67}(PO_4)_3$, which is a new variant of the alluaudite structure.

Since the mid-1950s, a number of compounds, including both phosphates ($Na_3In_2(PO_4)_3$ (9) and $NaMn_3(PO_4)(HPO_4)_2$ (10)) and arsenates ($NaCu_4(AsO_4)_3$ (11) and $AMn_4(AsO_4)_3$ (12) (A = Na, K)), have been reported which possess the common structure type of the well-known mineral alluaudite. Fisher (13) reported the first detailed crystal structure of alluaudite in 1955 and later proposed the general formula $X(2)X(1)M(1)M(2)(PO_4)_3$, where $X(2)$ and $X(1)$ are monovalent or divalent cations, respectively, and $M(1)$ and $M(2)$ are occupied by some distribution of Mn^{2+}, Fe^{2+}, Cu^{2+}, or Fe^{3+}. The ability of this structure type to include a variety of elements ranging from alkali metals, to transition metals, to main-group metals is observed. The compound reported here contains Fe^{3+} ions in

[1] To whom correspondence should be addressed. E-mail: kjoseph@clemson.edu

0022-4596/98 $25.00

a square-planar site which is normally vacant in classical alluaudite.

EXPERIMENTAL

Materials and Methods

All reagents were of analytical grade (Aldrich) and used without further purification. An X-ray powder diffraction continuous scan at room temperature was obtained at 0.25°/min with a Scintag XDS 2000 θ–θ powder diffractometer using Cu$K\alpha$ radiation ($\lambda = 1.5406$ Å). The Mössbauer spectra were measured on a monophasic powder, as determined by XRD, at 78 and 295 K on a conventional constant-acceleration spectrometer which utilized a room temperature rhodium matrix cobalt-57 source and was calibrated at room temperature with α-iron foil. The resulting spectra were least-squares fit with symmetric quadrupole doublets with Lorentzian lineshapes. No indication of any long-range magnetic order was observed in the spectra. The magnetic susceptibility was measured using a Quantum Design SQUID MPMS-5S magnetometer. Ground single-crystal samples (≈ 12 mg) were placed in a gel capsule sample holder which was suspended in a standard plastic drinking straw. The temperature- and field-dependent susceptibilities of the container were previously determined and their effect was negligible. The measurement was performed at 1.0 T in the temperature range 5.82–300 K. The thermal stability of the title phase was examined using a DuPont Instruments Thermal Analyst 2000 equipped with a high-temperature 1600 DTA cell adaptor. The ground crystals (≈ 19 mg total mass) were heated from 25 to 900°C at 5°C/min and then isothermed for 5 min, followed by cooling at 5°C/min to room temperature. After the DTA measurements, the sample was examined by powder X-ray diffraction. The optical band gap for a powder sample of $NaFe_{3.67}(PO_4)_3$ was determined from room temperature diffuse reflectance measurements over the 200- to 2500-nm range on a Shimadzu UV3100 spectrophotometer equipped with an integrating sphere attachment. Barium sulfate was used as the reflectance standard. The reflectance data were converted to relative absorption units using the Kubelka–Munk function (14), $\alpha/S = (1 - R)^2/2R$, where R is the reflectance at a given wavelength, α is the absorption coefficient, and S is the scattering coefficient. The scattering coefficient has been shown to be practically wavelength independent for particles larger than 5 μm, which is the case for the samples studied herein (15). The infrared absorption spectra of a single crystal was studied in the range 1200–400 cm^{-1} using a Nicolet Magna-IR Spectrometer 550 with a Spectra Tech IR-Plan Laboratory Microscope single-crystal attachment. An energy-dispersive X-ray analysis (EDAX) of a single crystal was obtained using a JEOL JSM-IC 848 scanning microscope equipped with a Princeton Gamma Tech (PGT) PRISM detector.

Synthesis

A mixture of 0.96 g of Fe_3O_4, 1.58 g of Na_3PO_4, and 1 mL of 85% H_3PO_4 (molar ratio of Na : Fe : P = 1 : 3 : 3) was added to 5 mL of distilled water in a 316 stainless steel HIP autoclave with standard cone and thread fittings and an internal volume of 10.1 mL. The reaction vessel was placed in a tube furnace and held at 375 °C for 72 hr before cooling to room temperature. The product was filtered, washed with water and acetone repeatedly, and dried in an oven at 62°C for 1 hr. The product contained dark green plate like crystals in 81% yield, whereas the remaining material consisted of tan polyhedral-shaped crystals which were determined to be $NaFe_3(PO_4)_3$ (16), the parent form of the mineral alluaudite. The two products could be easily separated by physical manipulation.

Structure Determination

A single crystal having dimensions of $0.06 \times 0.13 \times 0.02$ mm^3 was selected for indexing and intensity data collection on a Rigaku AFC7R four-circle diffractometer with graphite-monochromated Mo$K\alpha$ radiation ($\lambda = 0.71073$ Å). Crystallographic data for the title compound are summarized in Table 1. The unit cell parameters and orientation matrix were determined by a least-squares fit of 25 randomly located reflections between 11.82° and 20.97° in 2θ. Data

TABLE 1
Crystallographic Data for $NaFe_{3.67}(PO_4)_3$

Formula weight (g/mol)	512.7
Space group, Z	$C2/c$, 4
a (Å)	11.881(4)
b (Å)	12.564(3)
c (Å)	6.522(2)
β (°)	115.09(2)
V (Å^3)	881.7(5)
D_{calc} (g cm^{-3})	3.863
Temperature (K)	298
Radiation (graphite monochromated)	Mo$K\alpha$
Crystal shape, color, size (mm)	Plate, dark green, $0.06 \times 0.13 \times 0.02$
Linear absorption coefficient (mm^{-1})	6.594
Scan type/scan range (deg)	ω–2θ/0.68 + 0.35 tan θ
Scan speed (deg/min), rescans	6, ≤ 3
2θ min, max (deg)	3.5–50.0
Indices	$0 \to h$, $-k \to k$, $-l \to l$
Number of reflections measured	1654
Number of unique reflections, R_{int}	772, 0.0352
Number of reflections with $I > 2\sigma(I)$	670
Number of parameters	94
F(000)	989.41
Transmission factors	0.63–1.00
Final $R(F)$,[a] $R_w(F)$[b]	0.029, 0.033

[a] $R = \sum||F_o| - |F_c||/\sum|F_o|$.
[b] $R_w = [\sum w\{|F_o| - |F_c|\}^2/\sum w|F_o|^2]^{1/2}$; $w = 1/[\sigma^2(F) + 0.0005F^2]$.

were collected on a triclinic cell using an ω–2θ scan mode at 6°/min with up to three rescans. A total of 1654 reflections were collected with a maximum 2θ of 50° for the $h, \pm k, \pm l$ hemisphere. Final lattice parameters were derived from a least-squares fit of 25 reflections between 26.71° and 38.55° in 2θ. There was no detectable decay during the data collection as indicated by the intensities of the three standards measured every 100 reflections. The intensity data were corrected for Lorentz and polarization effects, and an empirical ψ-scan absorption correction (0.63–1.00) was applied. On the basis of systematic absences and successful solution and refinement of the structure, the space group was determined to be $C2/c$. Structure determination and refinement were performed on a Digital VAXstation 4000 using the SHELXTL-PLUS program package (17). The structure was solved by direct methods, SHELXS-86 (18), and refined by using full-matrix, least-squares techniques, with atomic scattering factors taken from the source programs. Direct methods were used to locate the metal atoms, and the remaining atoms were found from successive Fourier difference maps. All atoms were refined with anisotropic thermal factors. Atomic coordinates, bond angles and distances, and anisotropic thermal parameters are listed in Tables 2, 3, and 4, respectively.

When we remove Fe(3) from the refinement, the R factor increases to 19%, with about 28 electrons remaining in the electron density map. Fourier maps of this residual electron density show only minimal irregularities in the contours, thus supporting the lack of disorder on the site. When that site is refined at full occupancy as iron, the refinement R factor is 5.5%. Relative to Fe(1) and Fe(2), Fe(3) had rather large thermal motion so the occupancy and isotropic thermal parameter of Fe(3) were alternately refined to convergence and its occupancy was then fixed at 67% while allowing the thermal motion to vary anisotropically in the final cycles. The anisotropic thermal motion of Fe(3) may imply disorder along the a axis; however, refinement models allowing the x position to vary showed only a small shift and no improvement in thermal parameters. Also, long-exposure a- and c-axial photos showed no evidence of a supercell. Therefore, we believe the title phase to be non-stoichiometric with respect to Fe(3). This formulation is supported by other physical data (*vide infra*).

TABLE 2
Positional and Thermal Parameters[a] for $NaFe_{3.67}(PO_4)_3$

Atom	Wyckoff	x	y	z	U_{eq} (Å^2)
Na	4*e*	0.5000	0.4787(3)	−0.2500	0.031(1)
P(1)	4*e*	0.5000	0.2074(1)	−0.2500	0.010(1)
P(2)	8*f*	0.7328(1)	0.3911(1)	0.6255(2)	0.010(1)
Fe(1)	8*f*	0.7196(1)	0.3418(1)	0.1346(1)	0.010(1)
Fe(2)	4*e*	0.5000	0.2324(1)	0.2500	0.013(1)
Fe(3)	4*b*	1.0000	0.5000	0.5000	0.046(1)
O(1)	8*f*	0.5432(3)	0.2779(2)	−0.0375(4)	0.012(1)
O(2)	8*f*	0.6605(3)	0.3353(2)	0.3941(4)	0.015(1)
O(3)	8*f*	0.7787(3)	0.1769(2)	0.1874(4)	0.015(1)
O(4)	8*f*	0.6699(3)	0.5007(2)	0.1123(5)	0.014(1)
O(5)	8*f*	0.9011(3)	0.3690(3)	0.2564(5)	0.020(1)
O(6)	8*f*	0.3711(3)	0.0976(2)	0.1775(5)	0.018(1)

[a] Equivalent isotropic U parameters defined as 1/3 trace of orthogonalized U_{ij} tensor.

TABLE 3
Selected Interatomic Distances (Å) and Angles (deg) in $NaFe_{3.67}(PO_4)_3$

	[FeO_6] octahedra		
Fe(1)–O(1)	2.074(3)	Fe(1)–O(2)	2.091(4)
Fe(1)–O(3)	2.168(3)	Fe(1)–O(4)	2.069(3)
Fe(1)–O(5)	1.986(3)	Fe(1)–O(3A)	2.122(3)
O(1)–Fe(1)–O(2)	79.3(1)	O(1)–Fe(1)–O(3)	84.3(1)
O(2)–Fe(1)–O(3)	91.8(1)	O(1)–Fe(1)–O(4)	98.2(1)
O(2)–Fe(1)–O(4)	84.9(1)	O(3)–Fe(1)–O(4)	175.4(1)
O(1)–Fe(1)–O(5)	163.6(1)	O(2)–Fe(1)–O(5)	111.3(1)
O(3)–Fe(1)–O(5)	82.9(1)	O(4)–Fe(1)–O(5)	95.2(1)
O(1)–Fe(1)–O(3A)	81.5(1)	O(2)–Fe(1)–O(3A)	160.8(1)
O(3)–Fe(1)–O(3A)	85.0(1)	O(4)–Fe(1)–O(3A)	99.2(1)
O(5)–Fe(1)–O(3A)	87.2(1)		
Fe(2)–O(1)	2.218(3) × 2	Fe(2)–O(2)	2.161(3) × 2
Fe(2)–O(6)	2.196(3) × 2		
O(1)–Fe(2)–O(2)	74.7(1) × 2	O(1)–Fe(2)–O(6)	114.0(1) × 2
O(2)–Fe(2)–O(6)	164.0(1) × 2	O(1)–Fe(2)–O(1B)	150.1(2)
O(2)–Fe(2)–O(1B)	87.5(1) × 2	O(6)–Fe(2)–O(1B)	89.5(1) × 2
O(2)–Fe(2)–O(2B)	106.5(1)	O(6)–Fe(2)–O(2B)	87.8(1) × 2
O(6)–Fe(2)–O(6C)	79.1(2)		
	[FeO_4] square plane		
Fe(3)–O(5)	2.243(3) × 2	Fe(3)–O(6A)	2.354(3) × 2
O(5)–Fe(3)–O(6A)	78.6(1) × 2	O(5)–Fe(3)–O(5A)	180.0(1)
O(5)–Fe(3)–O(6B)	101.4(1) × 2	O(6A)–Fe(3)–O(6B)	180.0(1)
	[PO_4] tetrahedra		
P(1)–O(1)	1.538(3) × 2	P(1)–O(5B)	1.531(4) × 2
O(1)–P(1)–O(5B)	114.8(1) × 2	O(1)–P(1)–O(1A)	109.7(1)
O(1)–P(1)–O(5C)	107.6(1) × 2	O(5B)–P(1)–O(5C)	102.4(1)
P(2)–O(2)	1.552(3)	P(2)–O(3B)	1.543(3)
P(2)–O(4D)	1.536(3)	P(2)–O(6D)	1.538(3)
O(2)–P(2)–O(3B)	108.7(2)	O(2)–P(2)–O(4D)	106.8(1)
O(3B)–P(2)–O(4D)	109.3(2)	O(2)–P(2)–O(6D)	110.8(2)
O(3B)–P(2)–O(6D)	108.8(2)	O(4D)–P(2)–O(6D)	112.3(2)
	[NaO_8] polyhedra		
Na–O(1)	2.819(4) × 2	Na–O(4)	2.385(3) × 2
Na–O(2A)	2.908(4) × 2	Na–O(4A)	2.547(4) × 2

RESULTS

Structural Description

The title phase consists of $M(1)O_6$ and $M(2)O_6$ octahedra that share edges to form staggered chains stacked parallel to (100) planes. Equivalent chains are linked together in the y direction by vertex-sharing $P(1)O_4$ and

TABLE 4
Anisotropic Thermal Parameters[a] (Å^2) for $NaFe_{3.67}(PO_4)_3$

Atom	U_{11}	U_{22}	U_{33}	U_{12}	U_{13}	U_{23}
Na	0.020(1)	0.054(2)	0.016(1)	0	0.004(1)	0
Fe(1)	0.009(1)	0.012(1)	0.010(1)	0.001(1)	0.003(1)	0.000(1)
Fe(2)	0.011(1)	0.012(1)	0.015(1)	0	0.006(1)	0
Fe(3)	0.068(1)	0.018(1)	0.023(1)	0.003(1)	−0.008(1)	−0.003(1)
P(1)	0.009(1)	0.009(1)	0.008(1)	0	0.002(1)	0
P(2)	0.009(1)	0.010(1)	0.010(1)	0.000(1)	0.003(1)	−0.002(1)
O(1)	0.009(1)	0.017(2)	0.009(1)	−0.002(1)	0.002(1)	−0.003(1)
O(2)	0.020(2)	0.012(2)	0.012(1)	−0.005(1)	0.006(1)	−0.003(1)
O(3)	0.013(1)	0.020(2)	0.010(1)	0.001(1)	0.003(1)	0.002(1)
O(4)	0.014(1)	0.012(1)	0.017(1)	−0.002(1)	0.006(1)	0.003(1)
O(5)	0.019(2)	0.016(2)	0.023(2)	0.006(1)	0.006(1)	−0.003(1)
O(6)	0.012(2)	0.011(2)	0.033(2)	0.001(1)	0.010(1)	0.001(1)

[a] The general anisotropic thermal parameter expression is $\exp(-2\pi^2 [h^2a^{*2}U_{11} + \cdots + 2klb^*c^*U_{23}])$.

$P(2)O_4$ tetrahedra and square-planar FeO_4 units to form sheets oriented perpendicular to (001). The sheets are interconnected in the z direction by vertex-sharing oxygen atoms from the $P(2)O_4$ units. Projected down the c axis, these connected sheets produce one-dimensional channels located at the origin and the C-centered face. These are the sites in which the sodium cations reside. The geometry around the sodium atom can be described as bicapped trigonal prismatic.

A polyhedral representation of the structure viewed down the c axis is shown in Fig. 1. The open framework is built up from a complex arrangement of distorted of FeO_6 octahedra and PO_4 tetrahedra. There are three unique iron atoms in this structure. Fe(1) and Fe(2) are both in a distorted octahedral environment, with that of Fe(2) more distorted than that of Fe(1). The Fe–O bond distances range from 1.986(3) to 2.218(3) Å. The cis O–Fe(1)–O angles range from 79.3(1)° to 111.3(1)° whereas the O–Fe(2)–O angles range from 74.7(1)° to 114.0(1)°. This distortion is due in part to the rigidity of the PO_4 units that join adjacent FeO_6 chains, which run parallel to the a axis. Fe(1) sits on a general position while Fe(2) sits on a twofold rotation axis (Table 2). The Fe(1) atom forms edge-sharing octahedra with itself (Fig. 2) whose edge midpoints are inversion centers at $(\frac{1}{4}, \frac{1}{4}, 0)$ and $(\frac{3}{4}, \frac{3}{4}, 0)$, and each Fe(1) shares a common edge with the highly distorted Fe(2) octahedra to form chains of octahedra. This linking creates the staggered chains running parallel to the a axis. These chains are connected to similar neighboring chains in the y direction by vertex-sharing PO_4 tetrahedra as well as the square-planar Fe(3) (Fig. 3). The extended structure can be seen as parallel sheets which are interconnected along the c axis by PO_4 units (Figs. 1 and 4). The P–O distances are consistent

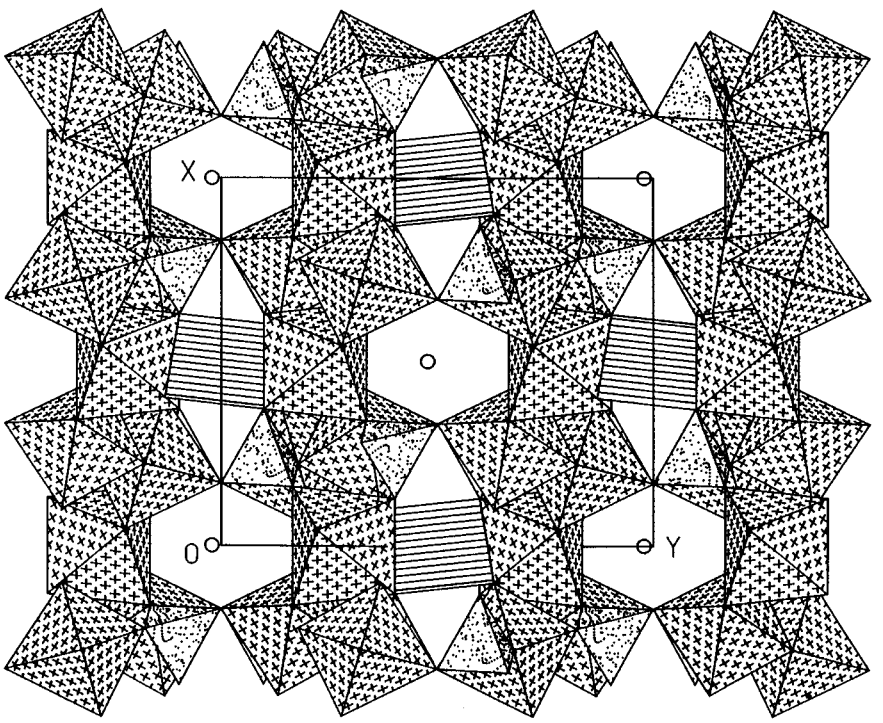

FIG. 1. Polyhedral representation of the $NaFe_{3.67}(PO_4)_3$ unit cell showing the open-framework channel structure propagating along [0, 0, 1]. The FeO_6 and PO_4 polyhedra are filled by lined and dotted patterns, respectively. The FeO_4 units at $(\frac{1}{2}, 0, 0)$ and $(0, \frac{1}{2}, 0)$ are drawn as parallel lines. The sodium ions occupy the cavities at the face center and corners of the unit cell are represented as unconnected open circles.

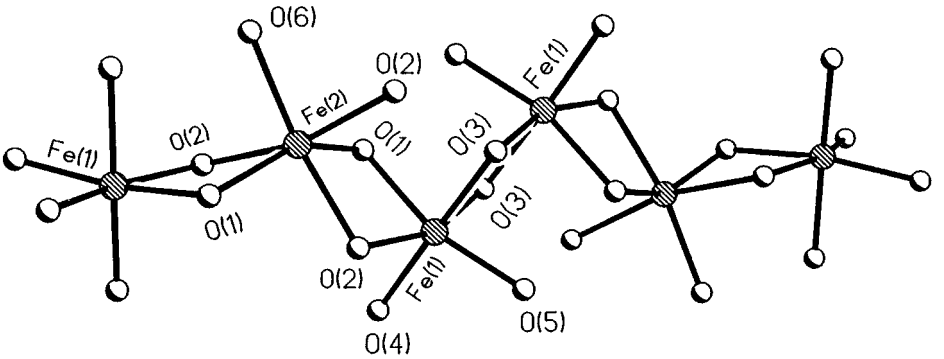

FIG. 2. Drawing of the kinked chains consisting of edge-sharing $Fe(1)O_6$–$Fe(2)O_6$ octahedra that run parallel to the *a* axis. The iron atoms are depicted as line-filled circles and the oxygen atoms are shaded circles.

with those typically seen in phosphates without hydrogen bonding (19–21), with average bond lengths of 1.535(4) Å for P(1) and 1.542(7) Å for P(2). The PO_4 groups within these chains serve as links which help make up the three-dimensional network of this structure.

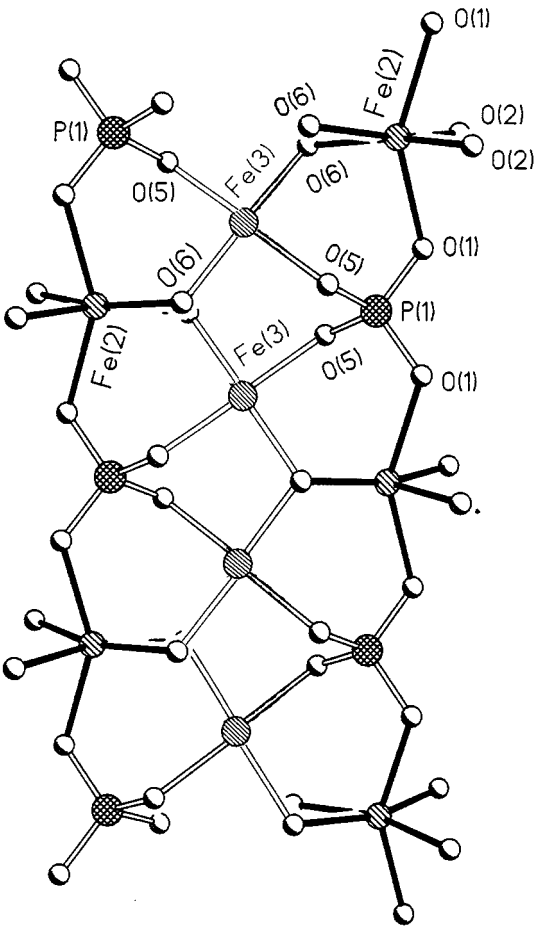

FIG. 3. View showing the connectivity of the extended network in $NaFe_{3.67}(PO_4)_3$ in the *bc* plane. The phosphorus atoms are depicted as cross-hatched circles, and iron and oxygen atoms are the same as in Fig. 2.

The third iron, Fe(3), sits on the *X*(1) site in the alluaudite structure and has an unusual square-planar geometry, with Fe–O distances of 2.243(3) and 2.354(3) Å, which are substantially longer than those in the iron octahedra. The next-nearest neighbors to Fe(3) are O(6) at 2.587 Å and O(5) at 2.925 Å. All four corners of the $Fe(3)O_4$ plane are vertex-sharing to the Fe(1) and Fe(2) octahedra (Fig. 4). A perfect planar environment around Fe(3) located on an inversion center is observed; however, there is distortion away from the expected 90° angles. This can be observed by the O(6a)–Fe(3)–O(5) angle of 78.6(1)° and the O(6)–Fe(3)–O(5)

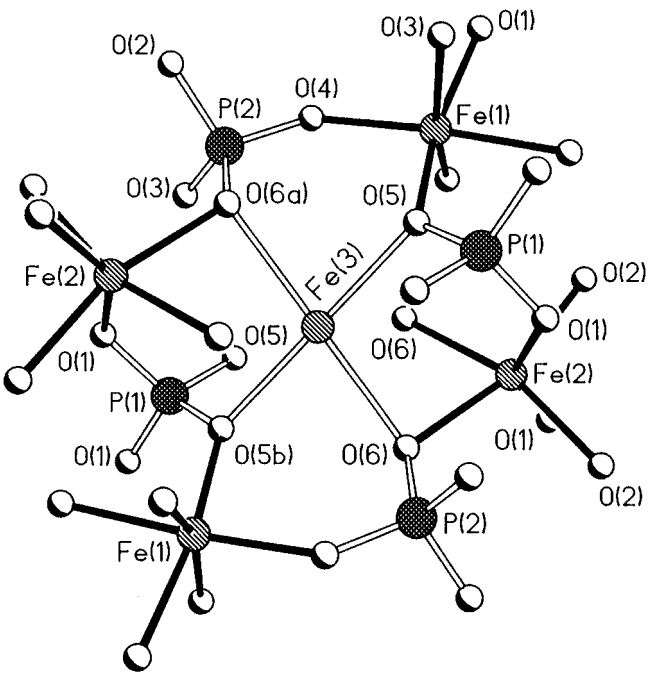

FIG. 4. View of the square-planar environment around the Fe(3) atom displaying the vertex-sharing make-up to $Fe(1)O_6$, $Fe(2)O_6$, $P(1)O_4$, and $P(2)O_4$ polyhedra observed down the *c* axis. The atom fillings are the same as in Figs. 2 and 3.

angle of 101.4(1)° and is most likely due to the phosphate packing environment around Fe(3) (Fig. 4).

There are several other examples in the literature of compounds whose structures are similar to the title phase with respect to the square-planar site, such as $NaCu_4(AsO_4)_3$ (11), $AgCu_4(AsO_4)_3$ (22), $Cu_{1.35}Fe_3(PO_4)_3$ (23), $NaCo_4(AsO_4)_3$ (24), and the mineral johillerite, $Na(Mg,Zn)_3Cu(AsO_4)_3$ (25). This square-planar site is normally unoccupied in alluaudite but has 2/3 occupancy in the title compound. The compound $NaMn_4(AsO_4)_3$, synthesized by Hwu *et al.* (12), also has a structure which is similar to that of the title compound; the difference lies in that the partially occupied "square-planar site" is occupied by distorted trigonal-prismatic MnO_6 units in which the Mn atom does not lie on the inversion center. In $NaMn_4(AsO_4)_3$ edge-shared trigonal-prismatic MnO_6 units make $[MnO_4]_\infty$ "columns" which run along the (001) direction.

The structure of $NaFe_{3.67}(PO_4)_3$ is similar to the alluaudite structure type of the pure iron containing mineral $NaFe_3(PO_4)_3$, with the one main difference being the partially filled channel in the title compound. In alluaudite there are two crystallographically unique channels, which are generally designated $X(1)$ and $X(2)$ (13). The oxygen coordination geometry about the $X(1)$ site at ($\frac{1}{2}$, 0, 0) is a distorted cube which shares faces with identical cubes to form channels running parallel to the c axis. They act as a template for cations such as the square-planar Fe^{3+} observed in the title phase. However, in the pure iron containing alluaudite structure, $NaFe_3(PO_4)_3$, this site is empty. This could account for the smaller b axis and c axis lengths in alluaudite of 12.328(1) and 6.500(1) Å, respectively, compared to 12.564(3) and 6.522(2) Å in the title compound. Also, having the $X(1)$ site occupied with Fe in $NaFe_{3.67}(PO_4)_3$ helps to account for the slightly larger unit cell volume in the title compound (ca. 4.7 $Å^3$) as compared to alluaudite. The second channel, referred to as the $X(2)$ site, is centered on the inversion center at the origin and is the position where the sodium ion resides in both alluaudite and the title phase. The coordination number of the alkali metal is eight with Na–O distances ranging from 2.385(3) to 2.908(4) Å (average = 2.665 Å). These pores have an approximately hexagonal opening in the ab plane with dimensions of 7.47×5.07 Å , respectively.

The oxidation states of all crystallographically unique atoms in the title compound were evaluated (Table 5) by using valence bond sum calculations (26). The values obtained for Fe(1), Fe(2), and Fe(3) are 2.35, 1.75, 0.94, respectively. The abnormally low value for Fe(3) can be explained by the existence of only very long contacts to four oxygen atoms. However, the oxidation states of the iron atoms are unequivocally determined by the Mössbauer and magnetic data. The other two metals, Fe(1) and Fe(2), show values similar to those for Mn(2) and Mn(3) in $NaMn_4(AsO_4)_3$, in which the authors rationalize this by the close metal–metal interactions within the Mn_2O_{10} dimers (12). The calculated bond valence sums for the oxygen atoms range from 1.73 to 2.20. These, along with the absence of any unusually long P–O bond distances, suggest the absence of any hydrogen atoms, forming bonds such as P–O–H or Fe–OH_2, in the title phase. This suggestion is also supported by the absence of O–H stretches in the 3400 to 3000 cm^{-1} region of the IR spectrum of the title compound.

TABLE 5
Bond Valence Sums for Atoms in $NaFe_{3.67}(PO_4)_3$

Atom	Valence	Atom	Valence
Na	0.91(1)	O(1)	1.97(1)
Fe(1)	2.35(1)	O(2)	1.99(1)
Fe(2)	1.75(1)	O(3)	1.88(1)
Fe(3)	0.94(1)	O(4)	2.20(1)
P(1)	5.00(2)	O(5)	2.04(1)
P(2)	4.90(3)	O(6)	1.73(1)

Physical Characterization of $NaFe_{3.67}(PO_4)_3$

The powder patterns of the title phase as well as $NaFe_3(PO_4)_3$ were calculated using the lattice parameters and atomic positions from the single-crystal results of these compounds, and all peaks correlated to the observed pattern. Because of the slight difference in the lattice parameters of the two compounds, the calculated powder patterns can be discriminated and clearly indicate that $NaFe_{3.67}(PO_4)_3$ is the major product. The other peaks can all be assigned to the minor presence of $NaFe_3(PO_4)_3$. Energy dispersive X-ray analysis (EDAX) on a single crystal qualitatively confirmed the presence of only sodium, iron, and phosphorus in approximately the correct ratios. The diffuse reflectance spectrum of the title compound confirmed the large band gap semiconducting nature of the compound, with a transition near 4 eV (Fig. 5). There is also a large transition near 1.1 eV, which may be a d–d transition of the iron sites but, because of its strength, may be more likely a LMCT band. Differential thermal analysis showed no thermal events below 900°C, suggesting a broad thermal stability region for this compound. The sample was weighed after the run and remained unchanged. The powder diffraction pattern also revealed no change after heating to 900°C. This thermal stability along with the ability for this structure type to accommodate many different sized cations makes it a possible candidate for an ion-exchange material. The infrared spectrum did show P–O vibrational frequencies associated with the $[PO_4]^{3-}$ groups (27) as a broad doublet of medium intensity with peaks centered at 1090 (s) and 900 (s) cm^{-1}, along with another band at 550 (m) cm^{-1}, which presumably is due to the iron–oxygen stretching vibrations.

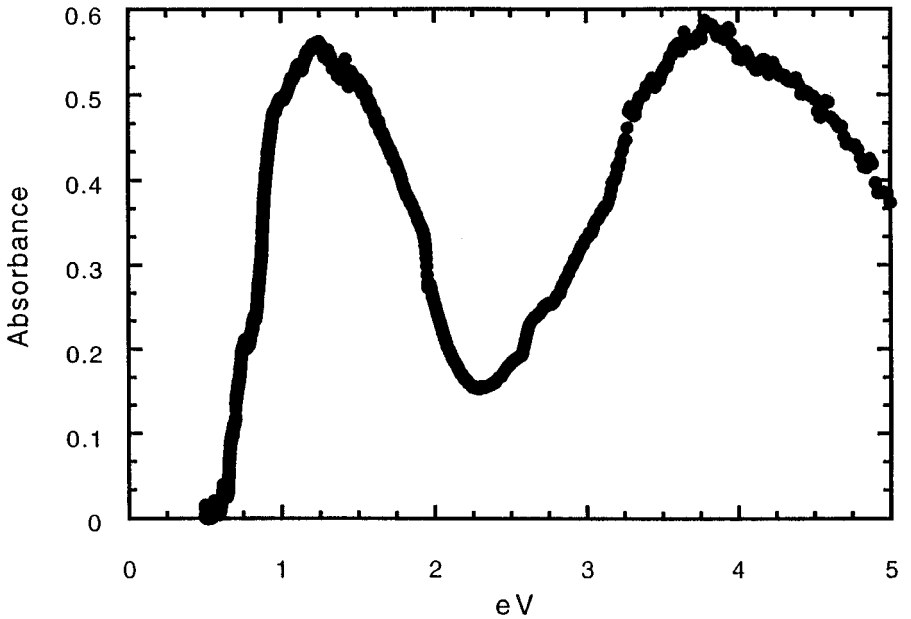

FIG. 5. Optical absorption spectrum of $NaFe_{3.67}(PO_4)_3$ plotted as arbitrary absorbance vs energy.

The Mössbauer spectra of $NaFe_{3.67}(PO_4)_3$ measured at 78 and 295 K are shown in Fig. 6 and the hyperfine parameters corresponding to the fits shown in this figure are given in Table 6. The fits, which consist of three symmetric quadrupole doublets, are assigned to the three different iron sites in $NaFe_{3.67}(PO_4)_3$ on the basis of their relative areas. As may be observed in Table 6, the relative areas of the doublets obtained from a least-squares fit agree well with those calculated from the structure and the stoichiometry of the compound. Although the fits are not unique, no other combination of three doublets led to fits which were better than those shown in Fig. 6 and had hyperfine parameters which were consistent with the structure and electronic properties of $NaFe_{3.67}(PO_4)_3$. As shown in Fig. 6, the fits are excellent but do show some distinct misfits at ca. 0 mm/s at 295 K and at ca. 2.7 mm/s at 78 K. These misfits could not be improved by any reasonable combination of asymmetric doublets and surely arise because of the partial occupation of the square-planar Fe(3) site and the consequent small variations in the environments observed at the Fe(1) and Fe(2) sites. Indeed, in view of the nonstoichiometric nature of $NaFe_{3.67}(PO_4)_3$, it is surprising how well resolved are the

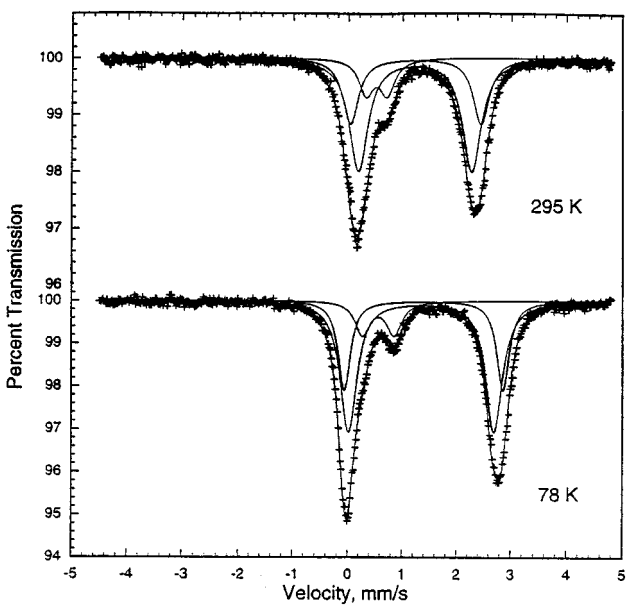

FIG. 6. Mössbauer spectrum of $NaFe_{3.67}(PO_4)_3$ at 295 K (top) and 78 K (bottom).

TABLE 6
Mössbauer Spectral Parameters for $NaFe_{3.67}(PO_4)_3$

Site	T (K)	δ^a (mm/s)	ΔE_Q (mm/s)	Γ (mm/s)	% Area observed	% Area expected[b]	Abs. area (‰ε)(mm/s)
Fe(1)	295	1.22	2.08	0.42	57.3	54.3	4.48
Fe(2)		1.24	2.40	0.36	28.6	27.2	
Fe(3)		0.50	0.38	0.34	14.1	18.5	
Fe(1)	78	1.36	2.67	0.36	57.6	54.3	6.05
Fe(2)		1.40	2.94	0.27	28.8	27.2	
Fe(3)		0.58	0.57	0.30	13.7	18.5	

[a] Relative to room temperature α-iron foil.

[b] The percentage area expected on the basis of the stoichiometry and the crystal structure.

observed spectra and how small are the observed doublet linewidths (Table 6).

The hyperfine parameters given in Table 6 are completely consistent with the electronic properties of $NaFe_{3.67}(PO_4)_3$ and with those obtained from related compounds (28–32). The isomer shifts, δ, and the quadrupole splittings, ΔE_Q, for the Fe(1) and Fe(2) sites are clearly indicative of iron (II) in highly distorted octahedral coordination environments (30, 31). Indeed, the larger observed quadrupole splitting for Fe(2) is consistent with the larger angular distortion from octahedral symmetry observed for this site (see Table 3 and earlier discussion) as compared with the Fe(1) site. The higher isomer shift observed for Fe(2), which has an average Fe–O bond distance of 2.192 Å, as compared to that of Fe(1), which has an average Fe–O bond distance of 2.085 Å, is consistent with the reduced covalency of the Fe(2) site.

The hyperfine parameters for the Fe(3) site are, as might be expected, rather unusual. The isomer shift for this site is completely consistent with the iron(III) oxidation state assigned to this iron and is very typical of iron(III) in related mixed-valent (28, 29) and non-mixed-valent compounds. More unusual is the rather small quadrupole splitting observed for Fe(3), the site which has a square-planar coordination environment. It may be that in this case the lattice and valence contributions to the electronic field gradient oppose each other, yielding a small quadrupole interaction, but the valence contribution would be expected to be rather small for an iron(III) ion.

It should be noted that although the percent areas of the three doublets agree rather well with the expected areas (Table 6), the relative area of the Fe(3) site is always less than the expected value. This is an indication that the recoil-free fractions for the three sites are not identical and as expected, the reduced coordination number of the square-planar Fe(3) site has the smallest recoil-free fraction. Although based on only two data points, and thus less reliable, the lattice properties of the three sites seem reasonable. The temperature dependence of the isomer shifts yields (33) effective recoil masses of 64, 56, and 110 g/mol for the Fe(1), Fe(2), and Fe(3) sites, respectively. The values for the Fe(1) and Fe(2) sites are very typical for ionic iron oxides and indeed the value for the Fe(1) site, with the shorter average bond distance, has the higher mass. The value for Fe(3) is quite high, perhaps because of its partial occupancy or, more likely, because the parameters for this weak doublet are less well determined. The temperature dependence of the isomer shift and the spectral absorption area yield (33) the Mössbauer temperature, a quantity which, like the Debye temperature, is related to the binding of an iron ion into the lattice. The resulting values for $NaFe_{3.67}(PO_4)_3$ are 290, 315, and 185 K for the Fe(1), Fe(2), and Fe(3) sites, respectively. Again the first two values are typical of iron(II) in oxide lattice sites, whereas the value for Fe(3) is lower, as would be expected for a square-planar site with a rather long average Fe–O bond distance of 2.298 Å.

Figure 7 shows the temperature dependence of the magnetic susceptibility and reciprocal susceptibility for $NaFe_{3.67}(PO_4)_3$. This compound displays Curie–Weiss behavior over a wide temperature range (18–300 K). A Curie constant (C) of 14.97 emu K^{-1} per formula unit was derived.

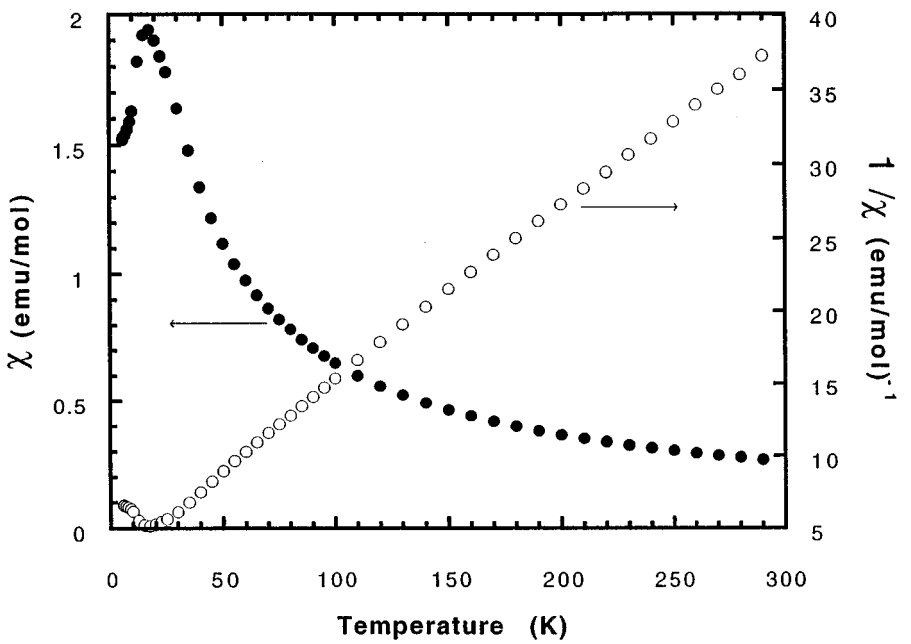

FIG. 7. Plot of magnetic susceptibility (solid circles) and reciprocal susceptibility (open circles) as a function of temperature for $NaFe_{3.67}(PO_4)_3$.

This value corresponds to an effective magnetic moment/Fe center of $\mu_{eff} = 5.7\ \mu_B$, which is between the expected spin-only values ($\mu = 4.90$ and $5.92\ \mu_B$) for Fe^{2+}/Fe^{3+}, respectively. This calculated value is slightly high but consistent with the assignment of high-spin, mixed-valent $Fe^{2+}(d^6)/Fe^{3+}(d^5)$ in octahedral and square-planar environments, respectively, in which the contribution from orbital angular momentum may be increasingly important. Potential Fe^{3+} impurities or the uncertainty of the occupancy of the square-planar Fe(3) site could also cause the effective moment to be slightly higher than expected. The observed Weiss constant has a negative value of $\Theta = -26$ K, which implies that the dominant interactions between neighbouring Fe atoms are weak and antiferromagnetic, and can be seen by the antiferromagnetic transition at $T_N = 18$ K (Fig. 7).

CONCLUSIONS

The title compound $NaFe_{3.67}(PO_4)_3$ has been prepared using the high-temperature/high-pressure hydrothermal technique and has been shown to be of the alluaudite structure type. The unique square-planar environment around the Fe(3) atom as well as the nonstoichiometry of this phase is confirmed by single-crystal X-ray crystallography, magnetic susceptibility, and Mössbauer studies.

ACKNOWLEDGMENTS

Financial support for this research from the National Science Foundation (Grants CHE-9102548 (J.K.) and DMR-9521739 (G.L.)) is gratefully acknowledged. We thank the Shiou-Jyh Hwu group for the use of their DTA, D. Hautot for assistance in obtaining the Mössbauer spectra, and Thomas Pennix Thrash at Rice University for collecting the magnetic susceptibility data on the title phase.

Supporting Information Available: Tables of detailed crystallographic data such as bond angles, figures of cation coordination, and the asymmetric unit are available upon request.

REFERENCES

1. (a) P. Moore and A. Kampf, *Z. Kristallogr.* **201,** 263 (1993); (b) P. Moore, *Am. Miner.* **57,** 397 (1972); (c) P. Moore, *Am. Miner.* **55,** 135 (1970); (d) P. Moore and T. Araki, *Inorg. Chem.* **15,** 316 (1976); (e) P. Moore, *in* "The Second International Congress on Phosphorus Compounds Proceedings," April 21–25, 1980, p. 105; (f) P. Moore and J. Shen, *Nature* **306,** 356 (1983).
2. (a) K. H. Lii and C. Huang, *J. Chem. Soc., Dalton Trans.* 571 (1995); (b) M. Gabelica-Robert, M. Goreaud, Ph. Labbe, and B. Raveau, *J. Solid State Chem.* **45,** 389 (1982); (c) M. Pintard-Screpel, F. D'Yvoire, and J. Durand, *Acta Crystallogr. Sect. C* **39,** 9 (1983); (d) D. Riou, Ph. Labbe, and M. Goreaud, *Eur. J. Solid State Inorg. Chem.* **25,** 215 (1988); (e) W. M. Reiff and C. Torardi, *Hyperfine Interact.* **53,** 403 (1990).
3. W. Meisel, H. J. Guttmann, and P. Gütlich, *Corros. Sci.* **23,** 1373 (1983).
4. S. Attali, B. Vigouroux, M. Lenzi, and J. Persia, *J. Catal.* **63,** 456 (1980).
5. J. B. Moffat, *Catal. Rev. Sci. Eng.* **18,** 199 (1978).
6. (a) M. S. Safonov, B. I. Lazoryak, S. B. Pozharskii, and S. B. Daschkov, *Dokl. Acad. Nauk.* **338,** 633 (1994); (b) B. I. Lazoryak, *in* "Fundamental Study of New Materials and Processes in the Substance," p. 54. Moscow University Press, Moscow, 1994.
7. P. Feng, X. Bu, and G. D. Stucky, *Nature* **388,** 735 (1997).
8. A. Rabenau, *Angew. Chem., Int. Ed. Engl.* **24,** 1026 (1985).
9. K. H. Lii and J. Ye, *J. Solid State Chem.* **131,** 131 (1997).
10. F. Leroux, A. Mar, C. Payen, D. Guyomard, A. Verbaere, and Y. Piffard, *J. Solid State Chem.* **115,** 240 (1995).
11. F. Pertlik, *Acta Crystallogr. Sect. C* **43,** 381 (1987).
12. T. A. Wardojo, R. Mackay, S. J. Hwu, C. J. O'Connor, and W. T. Pennington, *Inorg. Chem.*, accepted.
13. D. J. Fisher, *Am. Miner.* **40,** 1100 (1955).
14. W. W. Wendlandt and H. G. Hecht, "Reflectance Spectroscopy," Interscience Publishers, New York, 1966.
15. G. Kotum, "Reflectance Spectroscopy," Springer-Verlag, New York, 1969.
16. D. R. Corbin, J. F. Whitney, W. C. Fultz, G. D. Stucky, M. M. Eddy, and A. K. Cheetham, *Inorg. Chem.* **25,** 2279 (1986).
17. G. M. Sheldrick, SHELXTL-PLUS Crystallographic System, Release 4.11, Siemens Analytical X-ray Instruments Inc., Madison, WI, 1990.
18. G. M. Sheldrick, *in* "Crystallographic Computing 3" (G. M. Sheldrick, C. Krüger, and R. Goddard, Eds.), pp. 175–189. Oxford University Press, London, New York, 1985.
19. K. H. Lii, P. F. Shih, and T. M. Chen, *Inorg. Chem.* **32,** 4373 (1993).
20. P. Y. Feng, X. H. Bu, and G. D. Stucky, *J. Solid State Chem.* **129,** 328 (1997).
21. P. Y. Feng, X. H. Bu, and G. D. Stucky, *J. Solid State Chem.* **131,** 160 (1997).
22. H. Riffel, P. Keller, and H. Hess, *Z. Anorg. Allg. Chem.* **530,** 60 (1985).
23. T. E. Warner, W. Milius, and J. Maier, *J. Solid State Chem.* **106,** 301 (1993).
24. S. Khorari, A. Rulmont, and P. Tarte, *J. Solid State Chem.* **131,** 294 (1997).
25. P. Keller and H. Hess, *Neues Jahrb. Mineral. Monatsh.* **9,** 395 (1988).
26. I. D. Brown and D. Altermatt, *Acta Crystallogr. Sect. B* **41,** 244 (1985).
27. R. A. Nyquist and R. O. Kagel, "Infrared Spectra of Inorganic Compounds," 1st ed. Academic Press, New York, 1971.
28. G. J. Long and C. Gleitzer, *Hyperfine Interact.* **62,** 147 (1990).
29. M. Ijjaali, B. Malaman, G. Venturini, C. Gleitzer, G. J. Long, and F. Grandjean, *J. Phys. Condens. Matter* **3,** 9597 (1991).
30. P. D. Battle, A. K. Cheetham, C. Gleitzer, W. T. A. Harrison, G. J. Long, and G. Longworth, *J. Phys. C: Solid State Phys.* **15,** L919 (1982).
31. G. J. Long, A. K. Cheetham, and P. D. Battle, *Inorg. Chem.* **22,** 3012 (1983).
32. P. D. Battle, A. K. Cheetham, W. T. A. Harrison, and G. J. Long, *J. Solid State Chem.* **62,** 16 (1986).
33. R. D. Ernst, D. R. Wilson, and R. H. Herber, *J. Am. Chem. Soc.* **106,** 1646 (1984).